*fluids*

MDPI

*Article*

# Interfacial Evolution and Breakup Modes of Confined Fluid Threads in a Sudden Contraction Channel

**Wentao Wang [1], Luyao He [1], Shuang Li [2] and Xiaodong Chen [1,*]**

[1] School of Aerospace Engineering, Beijing Institute of Technology, Beijing 100081, China; 3120225025@bit.edu.cn (W.W.); 3120255140@bit.edu.cn (L.H.)
[2] Research Institute of System Engineering PLA Academy of Military Science, Beijing 100091, China; shuangli0611@163.com
* Correspondence: xiaodong.chen@bit.edu.cn

**Abstract**

The breakup of confined fluid threads in a circular sudden contraction microchannel was investigated by combining high-speed imaging with three-dimensional simulations using the Volume of Fluid (VOF) method. The effects of the capillary number $Ca$, normalized thread length $\overline{L} = L/(2R)$, lateral continuous phase flow rate $Q_3$, and rear wall contact on interfacial evolution and breakup were examined. At $Ca = O(10^{-5})$, representative experiments with $Q_1 = 0.60$ mL/h and $Q_2 = 1.70$ mL/h produced no breakup, rear-free breakup, rear-confined breakup, and multiple breakup at $Q_3 = 0.30$, 0.58, 0.80, and 1.00 mL/h, respectively. These values represent operating conditions for the observed modes rather than universal transition thresholds. At $Ca = O(10^{-4})$, the late-stage normalized curvature radii followed distinct fitted power laws. For rear-free breakup, $\overline{R}_1 \sim \overline{\tau}^{0.257}$ and $\overline{R}_m \sim \overline{\tau}^{0.182}$, whereas for rear-confined breakup, $\overline{R}_1 \sim \overline{\tau}^{0.350}$ and $\overline{R}_m \sim \overline{\tau}^{0.307}$. In the numerical simulations at a fixed mean fluid thread velocity of $9.23 \times 10^{-4}$ m/s and $\overline{L} = 1.3$, increasing $Q_3$ from 0.78 to 3.56 and 6.25 mL/h produced no breakup, rear-free breakup, and rear-confined breakup, respectively. The simulations reproduced the principal interfacial topology and event sequence observed experimentally and provided the three dimensional velocity and mean curvature fields. These results show that breakup is governed by the coupled effects of contraction geometry, external flow, thread length, and rear wall contact.

**Keywords:** confined fluid thread; sudden contraction microchannel; interfacial evolution; breakup mode; VOF method

Check for updates

Academic Editors: Wei Zhang, Zhentao Wang and Pengtao Yue

Received: 7 September 2026
Revised: 27 September 2026
Accepted: 3 October 2026
Published: 7 October 2026

**Copyright:** © 2026 by the authors. Licensee MDPI, Basel, Switzerland. This article is an open access article distributed under the terms and conditions of the Creative Commons Attribution (CC BY) license.

## 1. Introduction

Fluid thread breakup is governed by the competition between capillary, viscous, and inertial stresses. Plateau first documented the instability of cylindrical liquid columns, and Rayleigh showed that disturbances longer than the thread circumference grow through the Plateau–Rayleigh mechanism [1,2]. Eggers described the self similar approach to pinch off, while Papageorgiou related the late-stage evolution of a viscous thread to capillary and viscous stresses [3,4]. Lister showed that an outer viscous phase modifies breakup through viscosity ratio and interfacial stress coupling [5]. Driessen et al. further demonstrated that finite thread length and perturbation growth influence instability development [6]. The classical description therefore provides criteria for disturbance growth and for the final necking stage, but it assumes an unbounded or idealized thread. A solid wall restricts the admissible deformation and can maintain a lubricating film, while an abrupt contraction

additionally imposes a localized change in curvature and pressure. These studies establish the basis for interpreting neck growth, but do not address a moving interface constrained by a wall and a prescribed contraction.

Microfluidic work has quantified how confinement and imposed flow select breakup. Garstecki et al. found that the normalized dispersed phase length in the low capillary number squeezing regime follows $L/w = 1 + \alpha Q_d/Q_c$ [7], and van Steijn et al. subsequently connected dispersed phase size to the two phase flow rates and T junction geometry [8]. Anna et al. demonstrated controlled dispersion by flow focusing [9], whereas Guillot et al. showed that confinement changes the stability of a pressure driven biphasic jet at low Reynolds number [10]. Glawdel et al. identified a continuous change from pressure driven squeezing to shear assisted neck thinning as operating conditions vary [11]. The relation reported by Garstecki et al. is useful because it separates the contribution of the dispersed phase from that of the continuous phase, whereas the model of van Steijn et al. shows that the same flow rate ratio does not produce the same size when the junction geometry changes. The flow focusing experiments of Anna et al. further demonstrate that the upstream formation process determines the initial interface presented to a downstream disturbance. The results of Guillot et al. and Glawdel et al. indicate that confinement can change the relative importance of pressure and shear even at low Reynolds number. Taken together, these studies show that the same change in flow rate can alter both the amount of dispersed phase delivered to a junction and the stress balance that drives necking. They also indicate why a single capillary number is insufficient to describe a confined interface when the initial length and local transport history vary. These results establish flow rate and confinement as coupled controls of interfacial evolution.

Junction geometry and lateral forcing provide additional control. Bedram et al. related the daughter volume ratio in an asymmetric T junction to the initial length and outlet pressure difference [12]. Link et al. reported a geometrically mediated transition at a capillary number of order $10^{-3}$, consistent with the Rayleigh breakup condition [13]. Menetrier Deremble and Tabeling showed that the breakup response varies systematically with junction angle [14], while Che et al. demonstrated splitting by a hydrodynamic disturbance without a solid bifurcation [15]. Cubaud found that both viscosity ratio and capillary number affect deformation and breakup in symmetric cross flows [16], and Huerre et al. established that the lubrication film around a moving interface drains dynamically rather than being fixed by geometric clearance [17]. These studies provide complementary evidence that the interface responds to the spatial organization of the forcing, not only to its nominal magnitude. In particular, a lateral stream can change the pressure distribution at the front and rear of the interface, whereas an asymmetric outlet can shift the position of the neck before the final pinch off. The cited results cover symmetric and asymmetric junctions, but they generally treat the breakup site as a junction or outlet rather than as a fixed contraction embedded in the main channel. Thus, pressure, shear, geometry, and film drainage can act together near a breakup site, and their relative importance must be examined when a fluid thread is transported into a constriction.

Constrictions introduce a localized capillary constraint distinct from a branching junction. Roof related snap off to the local throat geometry in porous media, and Tsai and Miksis showed that a constricted capillary changes the curvature and pressure balance along a moving drop [18,19]. Datta et al. observed three dimensional breakup in a constricted porous medium [20], while Beresnev et al. related the breakup condition in a sinusoidally constricted capillary to constriction geometry and capillary stresses [21]. Wang et al. further showed that a constrictive microchannel can generate secondary dispersed structures after primary breakup [22]. These studies imply that a constriction can act both as a capillary barrier and as a location where the interface is reorganized. A circular sudden contraction is

especially relevant because the radius changes over a short axial distance while the interface remains connected to the upstream and downstream confinement. The resulting curvature redistribution cannot be inferred from a two dimensional centerline profile alone and may depend on the state of the rear interface at the contraction. These studies demonstrate the importance of constrictions, but do not resolve the coupled motion of a fluid thread, rear wall contact, and necking at a circular sudden contraction.

The closest precedents are the studies of moving fluid threads in serial junctions. Chen et al. identified a critical mean curvature radius of approximately $R_m \approx 0.71R$ for a confined thread [23]. Wang et al. found a transition near $Q_3 \approx 0.89$ mL/h and a minimum curvature radius of approximately $0.73R$ near breakup onset [24]. Wang et al. later distinguished nonbreakup, loosely confined breakup, and tightly confined breakup in asymmetric circular and square channels, with boundaries controlled by initial thread length and capillary number [25]. These results show that the radius of the interface and the initial thread length can provide useful indicators of breakup, but the reported thresholds were obtained without a fixed circular radius reduction in the main channel. The present device instead imposes a fixed circular reduction from $R$ to $R/2$ while lateral flow acts immediately upstream of the contraction. This configuration separates the contraction as a localized trigger from external flow as a control of neck development and permits breakup modes to be related to rear wall detachment and neck collapse. It also creates a direct link between the experimentally observed event sequence and the three dimensional redistribution of local curvature. Nevertheless, systematic studies of a fluid thread entering a circular sudden contraction remain limited, especially for the combined effects of contraction geometry, lateral transport, and rear wall contact.

We therefore investigate interfacial evolution and breakup modes in a circular sudden contraction microchannel with upstream radius $R = 1$ mm and downstream radius $R/2 = 500$ μm. Two serial flow focusing structures independently regulate the initial thread length and the lateral flow near the contraction, allowing the geometric and hydrodynamic controls to be varied separately. High-speed imaging records deformation, rear wall detachment, necking, and breakup, while the OpenFOAM interFoam solver with the VOF method [26] and PLIC reconstruction [27] resolves the three dimensional interface, capillary pressure, and necking chronology. The experiments establish the breakup mode map, and the simulations supply flow and curvature information that cannot be obtained directly from the projected images. The objective is to relate contraction geometry and external flow rate to breakup mode under confined asymmetric flow.

## 2. Materials and Methods

### *2.1. Experimental Methods*

The experimental arrangement and the geometry of the circular sudden contraction microfluidic device are shown schematically in Figure 1. Experiments were conducted in a polydimethylsiloxane (PDMS) device fabricated by replica molding. Five glass plates were assembled to form an open mold, and an iron rod with a diameter of 2 mm was positioned along the mold centerline to define the upstream main channel. PDMS prepolymer and curing agent (Sylgard 184, Dow Corning, Midland, MI, USA) were mixed at a mass ratio of 10:1, thoroughly stirred, degassed under vacuum, poured into the mold, and cured at 80 °C for 2 h. After curing, the PDMS block was removed from the mold, and the lateral channels were formed by inserting blunt needles from both sides. The PDMS block and a 25 mm × 75 mm glass substrate were treated with air plasma and subsequently bonded to obtain the completed microfluidic device.

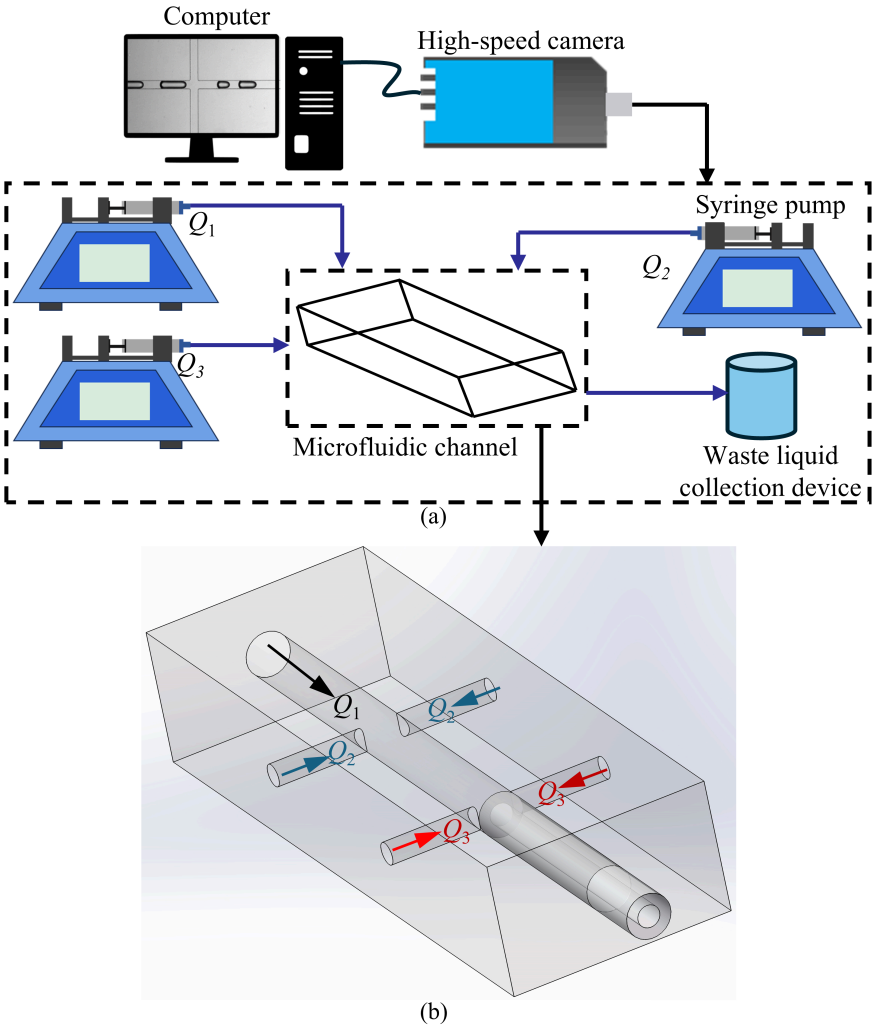



**Figure 1.** Experimental system and microfluidic device: (**a**) complete experimental arrangement comprising the computer, high-speed camera, syringe pumps, microfluidic device, and waste liquid collection unit; (**b**) sudden contraction microfluidic device, in which water enters the main channel at $Q_1$, while the two opposed upstream and downstream pairs of mineral oil inlets are each operated at $Q_2$ and $Q_3$, respectively.

During the experiments, the aqueous phase was introduced through the main channel inlet at a volumetric flow rate of $Q_1$, while mineral oil was supplied through four lateral channels as the continuous phase. The first opposed pair of lateral channels, each operated at $Q_2$, formed an upstream flow focusing junction and controlled the initial fluid thread length. The second opposed pair, each operated at $Q_3$, generated lateral oil flow immediately upstream of the sudden contraction and regulated the deformation and breakup of the fluid thread. A glass rod inserted into the downstream portion of the molded main channel produced the circular contraction. The upstream and downstream channel radii were $R = 1$ mm and $R/2 = 500$ μm, respectively, and the radius of each lateral channel was 500 μm.

Deionized water and mineral oil (M8410, Sigma–Aldrich, St. Louis, MO, USA) served as the fluid thread and continuous phases, respectively. Span 80 (S6760, Sigma–Aldrich, Shanghai, China) was added to the mineral oil at a mass fraction of 3%. To minimize adhesion of the aqueous fluid thread to the PDMS wall, Rain-X glass water repellent (Illinois Tool Works, Glenview, IL, USA) was injected into the channel and retained for 2 min. The channel was then rinsed with mineral oil and dried with compressed air. This treatment produced a strongly nonwetting wall condition for the aqueous phase

and improved the reproducibility of the thin oil film separating the fluid thread from the channel wall. The combined use of Span 80 in the oil phase and Rain-X treatment of the channel was intended to make the wall condition for the aqueous phase approach the limiting nonwetting state. A static contact angle was not measured in the assembled microchannel, so this treatment is used here to justify an idealized nonwetting boundary condition rather than to claim an exact measured contact angle. The kinematic viscosities of the aqueous and oil phases were 1.0 and 26.1 cSt, respectively, and their densities were 998.0 and 821.0 kg/m$^3$, respectively. The interfacial tension between water and oil was measured four times, yielding values of 2.1, 2.2, 2.4, and 2.6 mN/m. The mean value was 2.325 mN/m, with a sample standard deviation of 0.22 mN/m and a coefficient of variation of approximately 9.5%. The nominal value $\sigma = 2.3$ mN/m was used in the calculation of $Ca$. Because adsorption of Span 80 can cause the interfacial properties to vary with time, the reported capillary numbers should be interpreted as nominal values based on this measured mean.

The fluids were delivered from syringes by syringe pumps (Pump 11 Pico Plus Elite, Harvard Apparatus, Holliston, MA, USA). The manufacturer's specifications for this model report a flow rate accuracy of ±0.35% and a reproducibility of ±0.05% [28]. These values describe the pump specification and were not independently determined by gravimetric calibration of the complete fluid delivery system comprising the syringes, tubing, and microchannel. Interfacial evolution was recorded using a high-speed camera (pco.dimax HS1, PCO Imaging, Kelheim, Germany) at frame rates of up to 12,000 fps. The raw frames recorded by the high-speed camera had a size of 962 × 230 pixels (width × height). Each experimental condition was repeated three times. The camera was aligned with the main channel axis so that fluid thread translation, rear wall detachment, neck formation, and pinch off could be resolved from successive frames. Before each image sequence was acquired, the imposed flow rates were maintained until the system reached a statistically steady state.

The initial fluid thread length $L$ was normalized by the upstream channel diameter as

$$\overline{L} = \frac{L}{2R}. \tag{1}$$

The total lateral flow rate at the downstream junction was $2Q_3$. The capillary number was defined using the upstream channel cross-sectional area as

$$Ca = \frac{\mu_w 2Q_3}{\sigma \pi R^2}, \tag{2}$$

where $\mu_w$ is the dynamic viscosity of water, $\sigma$ is the water and oil interfacial tension, and $R$ is the upstream channel radius.

Following the curvature analysis of moving fluid threads in previous studies [24,25], the characteristic neck was defined as the thinnest cross-section along the thread axis. At the center of this section, two signed principal curvature radii, denoted by $R_1$ and $R_2$, were used to characterize the local interface geometry. The mean curvature radius was defined as

$$R_m = \frac{R_1 R_2}{R_1 + R_2}. \tag{3}$$

The signs of $R_1$ and $R_2$ follow the convention selected for the interface normal; therefore, a negative value of $R_2$ indicates an opposite local curvature orientation, or local concavity, rather than a negative geometric length. The normalized radii were defined as $\overline{R}_1 = R_1/R$, $\overline{R}_2 = R_2/R$, and $\overline{R}_m = R_m/R$, where $R$ is the upstream channel radius. Time was scaled by the upstream advection time, $2R/U_0$, where $U_0 = (Q_1 + 2Q_2)/(\pi R^2)$ is the nominal mean velocity upstream of the second junction. Accordingly, $\bar{t} = tU_0/(2R)$ and

the normalized time remaining before breakup is $\overline{\tau} = (t_c - t)U_0/(2R)$, where $t_c$ denotes the breakup time.

### *2.2. Numerical Methods*

#### 2.2.1. Governing Equations

Simulations in three dimensions were performed using the incompressible, immiscible two phase solver `interFoam` in OpenFOAM [29]. Both phases were modeled as Newtonian fluids, and the flow was assumed to be laminar because of the small channel dimensions and imposed flow rates. The mixture continuity and momentum equations were written as

$$\nabla \cdot \mathbf{u} = 0, \tag{4}$$

$$\frac{\partial(\rho \mathbf{u})}{\partial t} + \nabla \cdot (\rho \mathbf{u}\mathbf{u}) = -\nabla p + \nabla \cdot \left[\mu\left(\nabla \mathbf{u} + \nabla \mathbf{u}^{\mathsf{T}}\right)\right] + \rho \mathbf{g} + \mathbf{F}_\sigma, \tag{5}$$

where $\mathbf{u}$ is the velocity vector, $p$ is the pressure, $\rho$ and $\mu$ are the local mixture density and dynamic viscosity, respectively, $\mathbf{g}$ is the gravitational acceleration, and $\mathbf{F}_\sigma$ is the volumetric surface tension force. Surface tension was represented by the continuum surface force model [30]. The corresponding force was calculated as

$$\mathbf{F}_\sigma = \sigma \kappa \nabla \alpha, \tag{6}$$

where $\alpha$ denotes the aqueous phase volume fraction and $\kappa$ is the interface curvature, evaluated as

$$\kappa = -\nabla \cdot \left(\frac{\nabla \alpha}{|\nabla \alpha|}\right). \tag{7}$$

#### 2.2.2. Interface Capturing and Property Interpolation

The water and oil interface was captured using the VOF method [26]. The mixture properties were interpolated from the phase volume fractions according to

$$\rho = \alpha \rho_w + (1 - \alpha)\rho_o, \qquad \mu = \alpha \mu_w + (1 - \alpha)\mu_o, \tag{8}$$

where subscripts $w$ and $o$ denote water and oil, respectively. The conservative volume fraction equation is

$$\frac{\partial \alpha}{\partial t} + \nabla \cdot (\alpha \mathbf{u}) = 0. \tag{9}$$

To limit numerical diffusion across the interface, an additional compression flux was included, giving the transport equation solved in `interFoam` [29], which can be written as follows.

$$\frac{\partial \alpha}{\partial t} + \nabla \cdot (\alpha \mathbf{u}) + \nabla \cdot [\alpha(1 - \alpha)\mathbf{u}_r] = 0, \tag{10}$$

where $\mathbf{u}_r$ is the relative compression velocity. Cells with $\alpha = 1$ and $\alpha = 0$ contain water and oil, respectively, whereas $0 < \alpha < 1$ identifies interfacial cells. Piecewise Linear Interface Calculation (PLIC) was used to reconstruct a planar interface in each interfacial cell from the local volume fraction and interface normal [27]. This combination maintained phase volume conservation while reducing numerical smearing of the neck.

#### 2.2.3. Temporal and Spatial Discretization

The temporal term was discretized using a first order Euler scheme. The time step was adjusted automatically by setting `adjustTimeStep` to `yes`. The global Courant number and the interface Courant number were both limited to 0.2 through `maxCo` = 0.2 and `maxAlphaCo` = 0.2, respectively, while the time step was additionally bounded by `maxDeltaT` = $1 \times 10^{-3}$ s. Gradient terms were evaluated using Gauss linear interpolation, whereas convective terms were evaluated using a second order Gauss upwind scheme. Laplacian and diffusive terms were discretized using a Gauss linear scheme with orthogonal correction, while the pressure equation employed linear interpolation with nonorthogonal correction. The pressure and velocity fields were solved using the preconditioned conjugate gradient solver and `smoothSolver`, respectively. Pressure and velocity coupling was handled using the PIMPLE algorithm, which combines the relaxation iterations of the SIMPLE algorithm with the multiple pressure correction steps of the PISO algorithm. In the present simulations, `nCorrectors` was set to 3.

#### 2.2.4. Computational Domain, Boundary Conditions, and Mesh

The computational domain reproduced the circular sudden contraction geometry used in the experiments. The main channel diameters upstream and downstream of the contraction were 2 mm and 1 mm, respectively. Two opposed cylindrical side channels, each 1 mm in diameter, intersected the upstream main channel adjacent to the contraction. Mineral oil entered through the upstream main channel inlet at the combined flow rate $Q_1 + 2Q_2$ and through each lateral inlet at $Q_3$. An aqueous fluid thread of prescribed length was initialized in the upstream main channel, as illustrated in Figure 2.

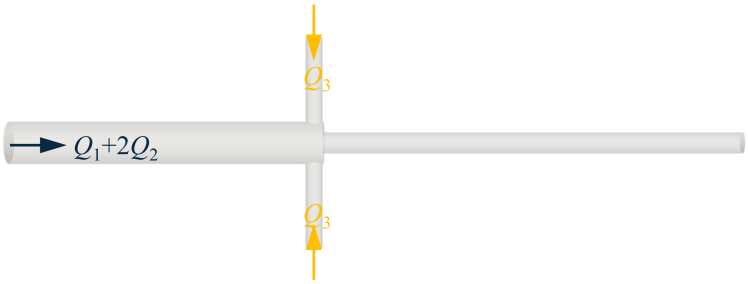



**Figure 2.** Computational domain for simulations in three dimensions. Mineral oil was supplied through the upstream main channel inlet at $Q_1 + 2Q_2$ and through each opposed side channel inlet at $Q_3$, while an aqueous fluid thread was initialized in the upstream main channel. The upstream and downstream main channel diameters were $2R$ and $R$, respectively.

Velocity boundary conditions corresponding to the prescribed volumetric flow rates were imposed at all inlets. A fixed pressure was specified at the downstream outlet, with zero gradient pressure conditions at the inlets. No slip conditions were applied to the solid walls. The water and wall contact angle was set to 180°. This value was selected as an idealized limiting representation of the strongly nonwetting experimental condition produced by the Span 80 containing oil phase and the Rain-X treatment, which were used to suppress adhesion of the aqueous phase and maintain an intervening oil film. Because the static contact angle was not measured in the assembled device, 180° is not interpreted as an exact experimental measurement, but as the numerical limit corresponding to the intended wall condition.

The mesh was generated in three stages. First, `blockMesh` was used to construct a hexahedral background mesh. Geometric features were then extracted with `surfaceFeatures`, and `snappyHexMesh` was used to generate a mesh conforming to the body geometry and

consisting of hexahedral and split hexahedral cells. The mesh convergence analysis and validation of the numerical simulations are presented in Section 3.3.

## 3. Results and Discussion

The results are arranged from experimental observation to numerical interpretation. The experimental results first establish the breakup modes and their dependence on capillary number and initial fluid thread length, followed by a quantitative analysis of curvature dynamics. The numerical analysis then assesses mesh resolution, validates the simulated rear-free breakup against the experiment, and examines the effects of $Q_3$ on interfacial topology, velocity structure, and mean curvature distribution.

### *3.1. Low Capillary Number Experiments on Breakup Modes and the Regime Map*

Figure 3 shows four representative interfacial responses obtained at fixed $Q_1 = 0.60$ mL/h and $Q_2 = 1.70$ mL/h. At $Q_3 = 0.30$ mL/h [Figure 3a], the leading end of the fluid thread entered the narrower downstream channel and the interface deformed near the contraction; however, the neck did not undergo sustained thinning, and the fluid thread passed through the junction without breakup. At $Q_3 = 0.58$ mL/h [Figure 3b], the rear of the fluid thread detached from the upstream wall before the minimum neck reached pinch off. Subsequent thinning therefore occurred after direct rear wall constraint had been removed, producing rear-free breakup. When $Q_3$ was increased to 0.80 mL/h [Figure 3c], the rear remained geometrically constrained near the contraction while the neck collapsed, and the event was classified as rear-confined breakup. At $Q_3 = 1.00$ mL/h [Figure 3d], more than one neck underwent pinch off, resulting in multiple breakup.

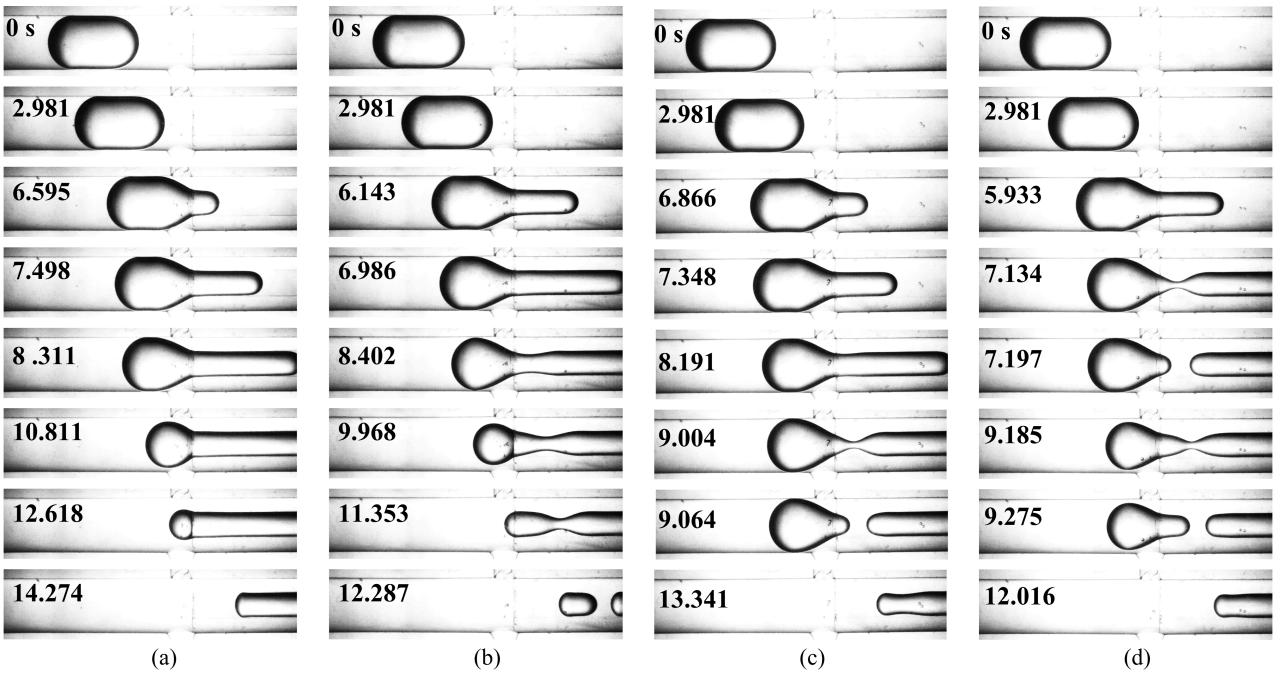



**Figure 3.** Representative interfacial evolution and breakup modes of confined fluid threads at low capillary number ($Q_1 = 0.60$ mL/h and $Q_2 = 1.70$ mL/h): (**a**) no breakup at $Q_3 = 0.30$ mL/h; (**b**) rear-free breakup at $Q_3 = 0.58$ mL/h; (**c**) rear-confined breakup at $Q_3 = 0.80$ mL/h; (**d**) multiple breakup at $Q_3 = 1.00$ mL/h.

The sequence of modes demonstrates that the contraction acts as a localized geometric trigger rather than merely as a passive change in cross-sectional area. As the fluid thread front enters the downstream channel, the interface must accommodate a reduction in radius from $R$ to $R/2$. The accompanying redistribution of the axial and transverse curvatures

produces a localized capillary pressure variation. At the smallest $Q_3$, capillary relaxation can balance the imposed deformation and restore a connected interface. Increasing $Q_3$ strengthens lateral compression and continuous phase displacement near the junction; once the local deformation becomes irreversible, curvature amplification and lubrication film drainage reinforce one another until pinch off. Thus, the sudden contraction localizes the development of the neck, whereas the final breakup mode is selected by the coupled effects of lateral forcing and rear wall contact.

The regime map in Figure 4 resolves the coupled dependence on $Ca$ and $\overline{L}$. For a given $\overline{L}$, the observed response progresses from no breakup to rear-free breakup, rear-confined breakup, and finally multiple breakup as $Ca$ increases. The plotted points cover approximately $1.73 \leq \overline{L} \leq 2.17$ and $0.8 \times 10^{-5} \lesssim Ca \lesssim 8.4 \times 10^{-5}$. For the representative condition with fixed flow rates in Figure 3, increasing $Q_3$ from 0.30 to 0.58, 0.80, and 1.00 mL/h corresponds to increases by factors of 1.93, 2.67, and 3.33 relative to the case without breakup and produces the sequence no breakup, rear-free breakup, rear-confined breakup, and multiple breakup. The colored point distributions shift toward lower $Ca$ as $\overline{L}$ increases. For example, the highest plotted point without breakup decreases from approximately $4.2 \times 10^{-5}$ at $\overline{L} \approx 1.73$ to approximately $2.6 \times 10^{-5}$ at $\overline{L} \approx 2.17$. These values describe the plotted point distributions rather than fitted transition thresholds. A larger $\overline{L}$ increases the extent of the fluid thread that interacts with the contraction and prolongs the residence of the rear interface near the junction, allowing deformation and continuous phase drainage to accumulate. The three dashed curves in Figure 4 are schematic guides to the eye used only to distinguish neighboring distributions of differently colored experimental points. They were drawn after all experimental points had been plotted and placed through gaps with low point density between neighboring distributions. No points were selected, discarded, or assigned additional weights. The curves are not statistical fits and do not represent quantitative transition boundaries or model predictions.

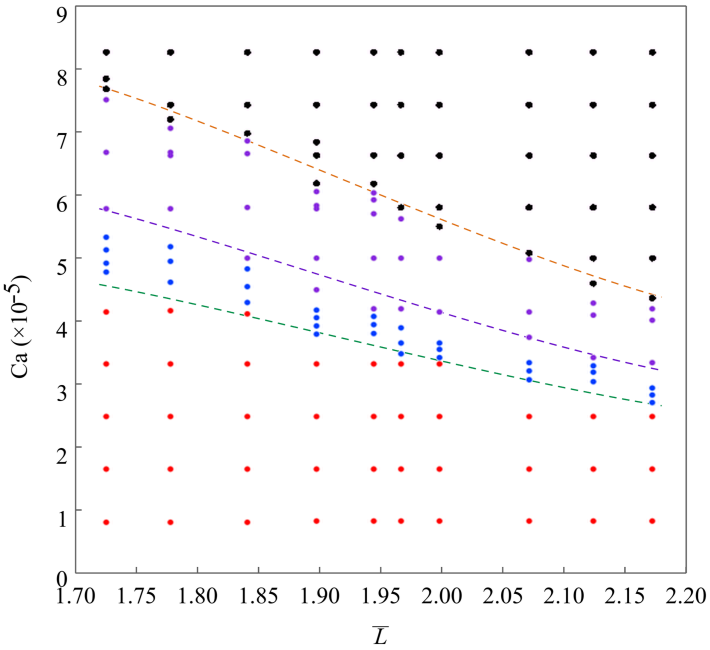



**Figure 4.** Breakup mode map for the low capillary number experiments. The abscissa is the normalized initial fluid thread length $\overline{L} = L/(2R)$, and the ordinate is $Ca$ in units of $10^{-5}$. Red, blue, magenta, and black symbols denote no breakup, rear-free breakup, rear-confined breakup, and multiple breakup, respectively; the three dashed curves are schematic guides to the eye used to distinguish the distributions of differently colored experimental points and are not statistical fits or quantitative transition boundaries.

At $Ca = O(10^{-5})$, interfacial tension remains sufficiently strong for a substantial interval of quasistatic accommodation. The distinction between breakup modes is therefore determined not only by the magnitude of the applied forcing but also by the order of the interfacial events. Rear detachment before irreversible neck collapse leads to rear-free breakup, whereas persistent rear contact maintains coupling between the neck, wall film, and contraction geometry and produces rear-confined breakup. Multiple breakup appears only after the forcing is sufficiently strong to destabilize more than one localized region. The breakup map at low *Ca* thus supports a description based on the two parameters *Ca* and $\overline{L}$, with rear wall contact providing the kinematic criterion that separates the two single breakup modes.

### *3.2. Higher Capillary Number Experiments on Interfacial Evolution and Curvature Dynamics*

Building on the low capillary number results, the following section examines the corresponding interfacial responses and curvature dynamics at higher *Ca*, where lateral transport and shear are more pronounced.

The high capillary number image sequences in Figure 5 contain the three modes used for the subsequent geometric analysis. Under the condition in Figure 5a, the fluid thread deformed markedly as it approached the contraction but remained connected. The rear-free breakup sequence in Figure 5b shows rear detachment followed by rapid necking downstream of the geometric constraint. In contrast, the rear-confined case in Figure 5c retained contact near the contraction during the late stage of neck collapse. Compared with the sequences at low *Ca*, the intervals between pronounced deformation and the final state were shorter, indicating that advection and lateral forcing had become more influential relative to capillary relaxation.

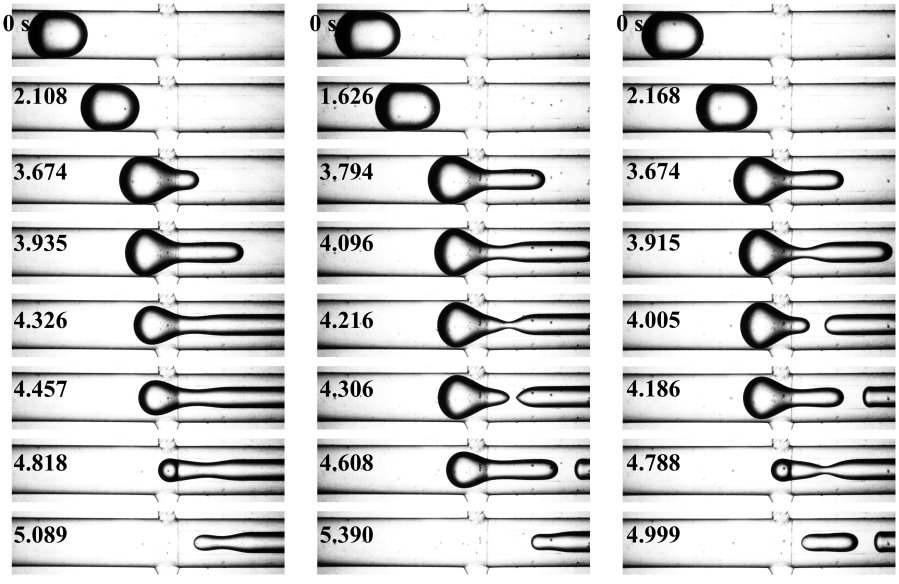



**Figure 5.** High-speed image sequences of fluid thread evolution at higher capillary number: (**a**) no breakup at $Q_1 = 0.30$ mL/h, $Q_2 = 5.85$ mL/h, and $Q_3 = 1.90$ mL/h; (**b**) rear-free breakup at $Q_1 = 0.80$ mL/h, $Q_2 = 5.60$ mL/h, and $Q_3 = 2.30$ mL/h; (**c**) rear-confined breakup at $Q_1 = 0.40$ mL/h, $Q_2 = 5.80$ mL/h, and $Q_3 = 3.20$ mL/h.

Within the investigated experimental regime, multiple breakup was observed only for the specific combination of capillary number, initial fluid thread length, and flow rates represented by Figure 3d. In contrast, the conditions at higher capillary numbers shown in Figure 5 did not exhibit additional breakup events over the tested parameter

range. These results characterize the breakup mode selection observed under the present experimental conditions.

Figure 6 shows that the no breakup, rear-free breakup, and rear-confined breakup point distributions remain ordered with increasing $Ca$. The plotted points cover approximately $1.23 \leq \overline{L} \leq 1.37$ and $0.2 \times 10^{-4} \lesssim Ca \lesssim 2.9 \times 10^{-4}$. The representative sequences in Figure 5 span $Q_3 = 1.90$, 2.30, and 3.20 mL/h, with the corresponding responses of no breakup, rear-free breakup, and rear-confined breakup. Thus, the largest $Q_3$ is approximately 1.68 times the smallest value, although these three examples also have different $Q_1$ and $Q_2$ and therefore do not define a threshold based on a single parameter. The two dashed curves are schematic guides to the eye placed in gaps with low point density between neighboring distributions after all experimental points had been plotted. They are used only for visual separation and should not be interpreted as quantitative boundaries for onset or transitions between modes. The point distributions shift toward lower $Ca$ as $\overline{L}$ increases, indicating that longer fluid threads are destabilized under weaker lateral forcing. The broader breakup domain at $Ca = O(10^{-4})$ indicates that lateral transport and shear contribute more strongly to neck collapse; it does not imply that geometry becomes secondary. The contraction and the rear contact state continue to determine whether the resulting breakup is rear-free or rear-confined.

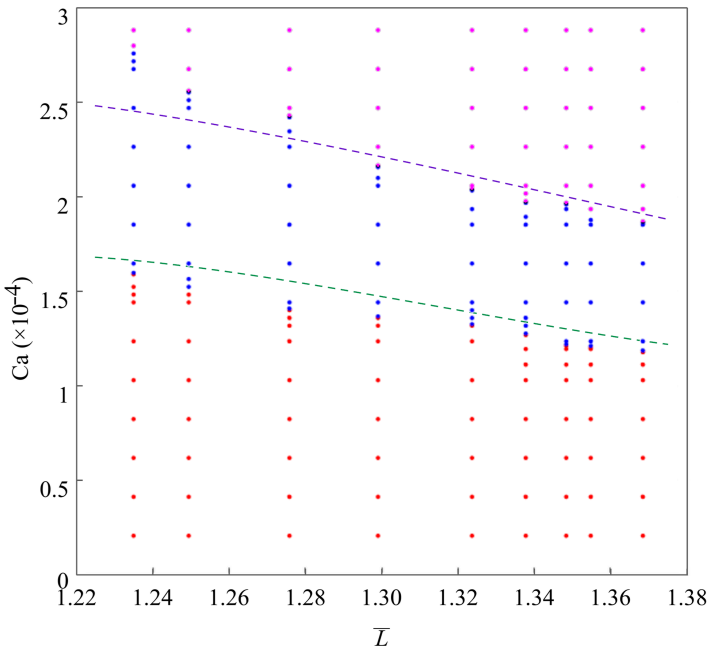



**Figure 6.** Breakup mode map for the higher capillary number experiments. The abscissa is the normalized initial fluid thread length $\overline{L} = L/(2R)$, and the ordinate is $Ca$ in units of $10^{-4}$. Red, blue, and magenta symbols denote no breakup, rear-free breakup, and rear-confined breakup, respectively; the two dashed curves are schematic guides to the eye used to distinguish the distributions of differently colored experimental points and are not statistical fits or quantitative transition boundaries.

In the no breakup case, all three measures vary smoothly and remain finite, consistent with a bounded deformation followed by capillary readjustment. Both breakup cases exhibit a pronounced late-stage change in the principal radii, demonstrating that the neck becomes increasingly anisotropic as pinch off is approached. The rear-confined case evolves over the shortest normalized interval, which is consistent with sustained coupling between the local curvature field and the sudden contraction.

The logarithmic plots in Figure 7d,e express the late-stage data in terms of the normalized remaining time $\overline{\tau}$. The power law $\overline{R} = A\overline{\tau}^{\beta}$ was fitted in logarithmic coordinates, $\ln \overline{R} = \ln A + \beta \ln \overline{\tau}$. The coefficient of determination $R^2$ was calculated in logarithmic

coordinates, and the uncertainty of $\beta$ was evaluated from the slope standard error and the corresponding 95% confidence interval based on the Student $t$ distribution. For rear-free breakup, the fitting interval was $0.020 \leq \overline{\tau} \leq 1.00$. The fit for $\overline{R}_1$ gave $\beta = 0.257$, $R^2 = 0.9982$, a standard error of 0.00125, and a 95% confidence interval of 0.2545–0.2595. The fit for $\overline{R}_m$ gave $\beta = 0.182$, $R^2 = 0.9869$, a standard error of 0.00245, and a 95% confidence interval of 0.1771–0.1869. For rear-confined breakup, the fitting interval was $0.010 \leq \overline{\tau} \leq 0.30$. The fit for $\overline{R}_1$ gave $\beta = 0.350$, $R^2 = 0.9986$, a standard error of 0.00225, and a 95% confidence interval of 0.3454–0.3546. The fit for $\overline{R}_m$ gave $\beta = 0.307$, $R^2 = 0.9981$, a standard error of 0.00236, and a 95% confidence interval of 0.3022–0.3118. The larger effective exponents in the rear-confined mode indicate a stronger late-stage dependence of the characteristic radii on the remaining time. These exponents and their confidence intervals are specific to the present geometry, radius definitions, data sampling, and fitting intervals and should not be interpreted as universal similarity exponents.

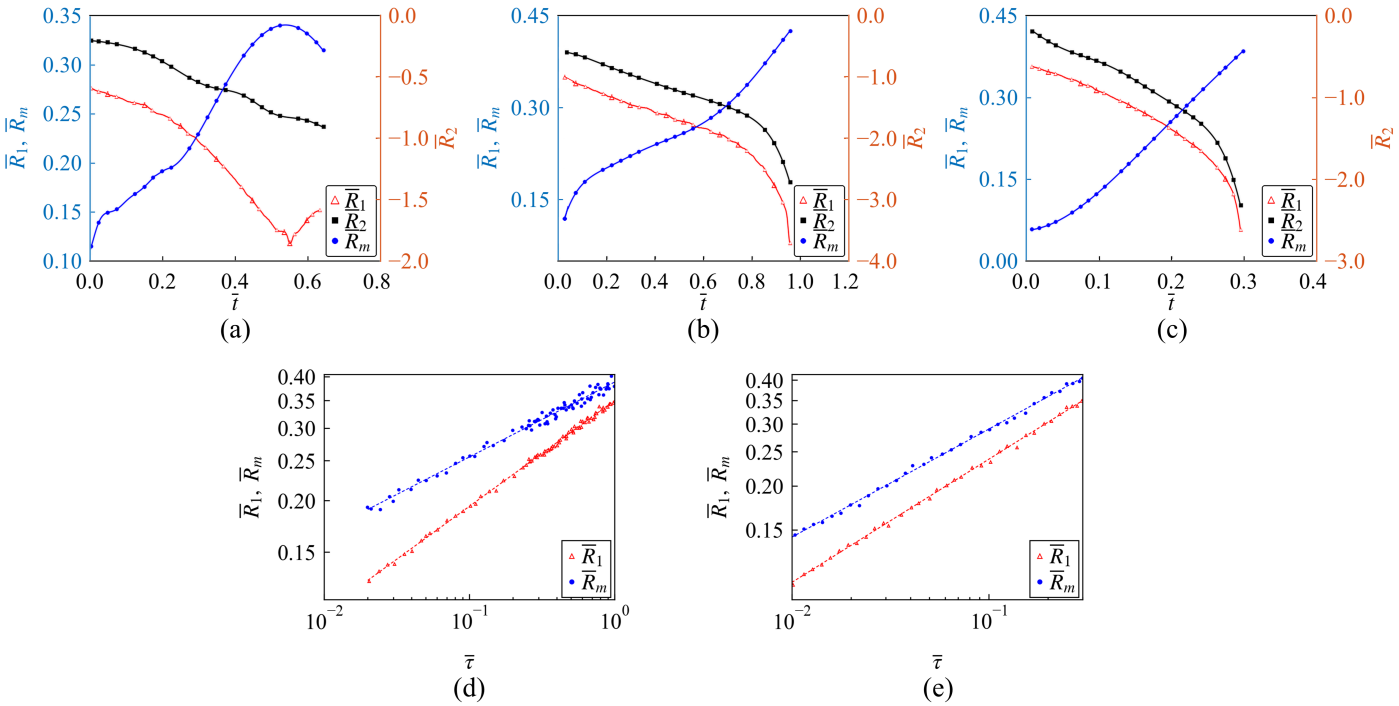



**Figure 7.** Normalized curvature radius dynamics measured from the higher capillary number experiments: (**a**) temporal evolution of $\overline{R}_1$, $\overline{R}_2$, and $\overline{R}_m$ for no breakup; (**b**) corresponding evolution for rear-free breakup; (**c**) corresponding evolution for rear-confined breakup; (**d**) late-stage scaling for rear-free breakup, $\overline{R}_1 \sim \overline{\tau}^{0.257}$ and $\overline{R}_m \sim \overline{\tau}^{0.182}$; (**e**) late-stage scaling for rear-confined breakup, $\overline{R}_1 \sim \overline{\tau}^{0.350}$ and $\overline{R}_m \sim \overline{\tau}^{0.307}$. The logarithmic fits in (**d**,**e**) used $0.020 \leq \overline{\tau} \leq 1.00$ and $0.010 \leq \overline{\tau} \leq 0.30$, respectively; the corresponding goodness of fit and exponent uncertainties are reported in the text.

### *3.3. Numerical Resolution and Experimental Validation*

The experiments define the observable breakup states and curvature response at higher *Ca*, but they cannot directly resolve the internal three-dimensional flow or the complete surface curvature distribution. Numerical simulations are therefore introduced to validate the selected experimental breakup sequence and to provide these additional flow and curvature fields.

Figure 8 compares simulations with 25, 30, and 35 cells across the diameter of the downstream narrow channel, which is the small channel formed by the sudden contraction and has a diameter of 1 mm, numerically equal to the upstream radius $R$, for the rear-free breakup condition in Figure 5b. All three resolutions reproduce neck formation and daughter droplet production. The mesh with 25 cells predicts breakup at approximately

11.00 s, whereas the meshes with 30 and 35 cells both predict breakup at approximately 11.05 s and yield closely matching interface profiles. Thus, the 0.05 s difference occurs between the meshes with 25 and 30 cells, while the meshes with 30 and 35 cells give the same breakup time at the temporal resolution shown.

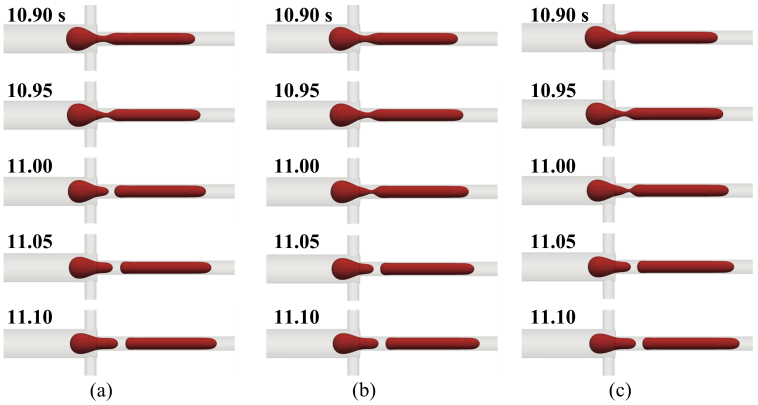



**Figure 8.** Mesh convergence study for the rear-free breakup condition $Q_1 = 0.80$ mL/h, $Q_2 = 5.60$ mL/h, and $Q_3 = 2.30$ mL/h, with the cell counts specified across the diameter of the downstream narrow channel (1 mm, equal to the upstream radius $R$): (**a**) 25 cells; (**b**) 30 cells; (**c**) 35 cells.

As an additional quantitative convergence metric, the axial displacement of the rightmost point of the fluid thread interface was extracted from each simulated sequence over the interval from 10.90 to 11.10 s. The extracted displacements for the meshes with 25, 30, and 35 cells were 1.46, 1.46, and 1.49 mm, respectively. These three displacement values are close to one another, with a maximum relative difference of approximately 2.0% among the three meshes. This small variation supports the practical convergence of the mesh results. Considering both the breakup time and the axial displacement of the rightmost point of the fluid thread, the mesh with 30 cells across the diameter of the downstream narrow channel was selected for all subsequent simulations. This mesh contained approximately 1.8 million cells throughout the computational domain.

The numerical sequence in Figure 9 was compared directly with the experimental rear-free breakup sequence in Figure 5b under the same flow rate conditions. The simulation and experiment exhibit some differences. Accordingly, the comparison is intended to assess the consistency of the breakup morphology and relative event timing rather than to claim exact pointwise agreement. The validation simulation used $Q_1 = 0.80$ mL/h, $Q_2 = 5.60$ mL/h, and $Q_3 = 2.30$ mL/h, together with the same nominal fluid properties and interfacial tension as the corresponding experiment. The simulation was performed at $Ca = 1.8 \times 10^{-4}$. Figure 9 compares three representative states selected according to the interface morphology. The time coordinate was shifted separately for the experiment and simulation according to $t' = t - t_b$, where $t_b$ denotes the first resolvable complete breakup in each sequence. Thus, the breakup state is defined as $t' = 0$, and states before breakup have negative values. In both datasets, the fluid thread develops an elongated neck near the contraction, the rear interface detaches from the upstream wall, and the neck subsequently collapses. Throughout the breakup process, the overall morphology of the fluid thread remains consistent between the simulation and experiment, including elongation, neck formation, rear detachment, and final separation. The comparison therefore confirms the same breakup topology and event order, although the detailed interface contour and neck contraction rate are not identical. These differences may be associated with the idealized numerical contact angle, the unresolved thickness and dynamics of the experimental oil film, variation in interfacial tension with time, differences between the initialized and

experimental interface states, and image based time registration. The simulation is therefore used to interpret the three-dimensional flow and curvature fields and is not presented as an exact pointwise reconstruction of the experimental contour.

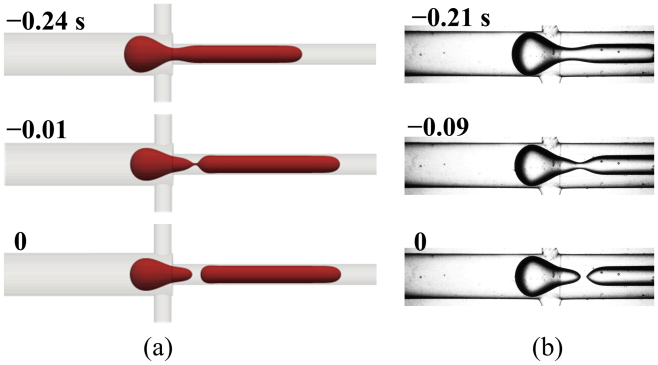



**Figure 9.** Comparison between the numerical and experimental rear-free breakup sequences under $Q_1 = 0.80$ mL/h, $Q_2 = 5.60$ mL/h, and $Q_3 = 2.30$ mL/h, corresponding to $Ca_{\mathrm{sim}} \approx 1.8 \times 10^{-4}$: (**a**) numerical interface states at $t' = -0.24$, $-0.01$, and 0 s; (**b**) experimental interface states at $t' = -0.21$, $-0.09$, and 0 s. Here, $t' = 0$ denotes the first resolvable complete breakup in each sequence.

### *3.4. Effect of the Lateral Flow Rate on Breakup and Flow Structure*

After validation against the selected rear-free breakup experiment, the numerical model is used to isolate the role of $Q_3$ while the mean fluid thread velocity and initial length are held fixed.

The simulations were conducted at a fixed mean fluid thread velocity of $9.23 \times 10^{-4}$ m/s and an initial length of $\overline{L} = 1.3$. As shown in Figure 10a, $Q_3 = 0.78$ mL/h produces a finite deformation near the contraction, but the interface remains connected and the fluid thread ultimately traverses the junction. At $Q_3 = 3.56$ mL/h [Figure 10b], the rear clears the upstream constraint before neck collapse, resulting in rear-free breakup. Further increasing the lateral flow to $Q_3 = 6.25$ mL/h [Figure 10c] confines the neck close to the contraction and produces rear-confined breakup. Relative to the case without breakup, these values represent increases in $Q_3$ by factors of 4.56 and 8.01, respectively, while the value for the rear-confined breakup case is 1.76 times that for the rear-free breakup case. Because the mean translation velocity and initial length are unchanged, this controlled sequence demonstrates that $Q_3$ independently controls the local transverse forcing and hence the transition among the three modes.

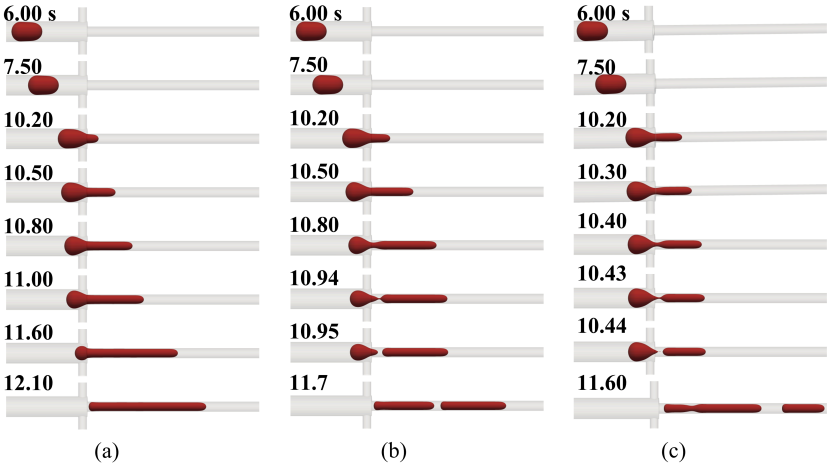



**Figure 10.** Numerical interfacial evolution at a fixed mean fluid thread velocity of $9.23 \times 10^{-4}$ m/s and $\overline{L} = 1.3$: (**a**) no breakup at $Q_3 = 0.78$ mL/h; (**b**) rear-free breakup at $Q_3 = 3.56$ mL/h; (**c**) rear-confined breakup at $Q_3 = 6.25$ mL/h.

The center plane velocity magnitude and streamlines at selected stages in Figure 11 provide a flow field interpretation of the interfacial responses shown in Figure 10. Under the no breakup condition, the continuous phase accelerates as the fluid thread enters the downstream channel, while the recirculating regions remain distributed around the rear interface and no persistent localized neck develops. The fluid thread therefore passes through the contraction without breakup. For rear-free breakup, streamline convergence and the local velocity gradient become increasingly concentrated around the neck at $t = 10.94$ and 10.95 s after the rear interface has moved away from the upstream geometric constraint. The neck is consequently drawn downstream before pinch off. For rear-confined breakup, the high-velocity region remains localized adjacent to the contraction from $t = 10.40$ to 10.44 s. The opposed lateral inflows maintain strong focusing of the continuous phase around the neck, leading to rapid thinning and breakup close to the geometric discontinuity. These selected flow fields demonstrate that increasing $Q_3$ strengthens and localizes the velocity gradient around the neck and thereby promotes the transition from no breakup to rear-free breakup and ultimately to rear-confined breakup.

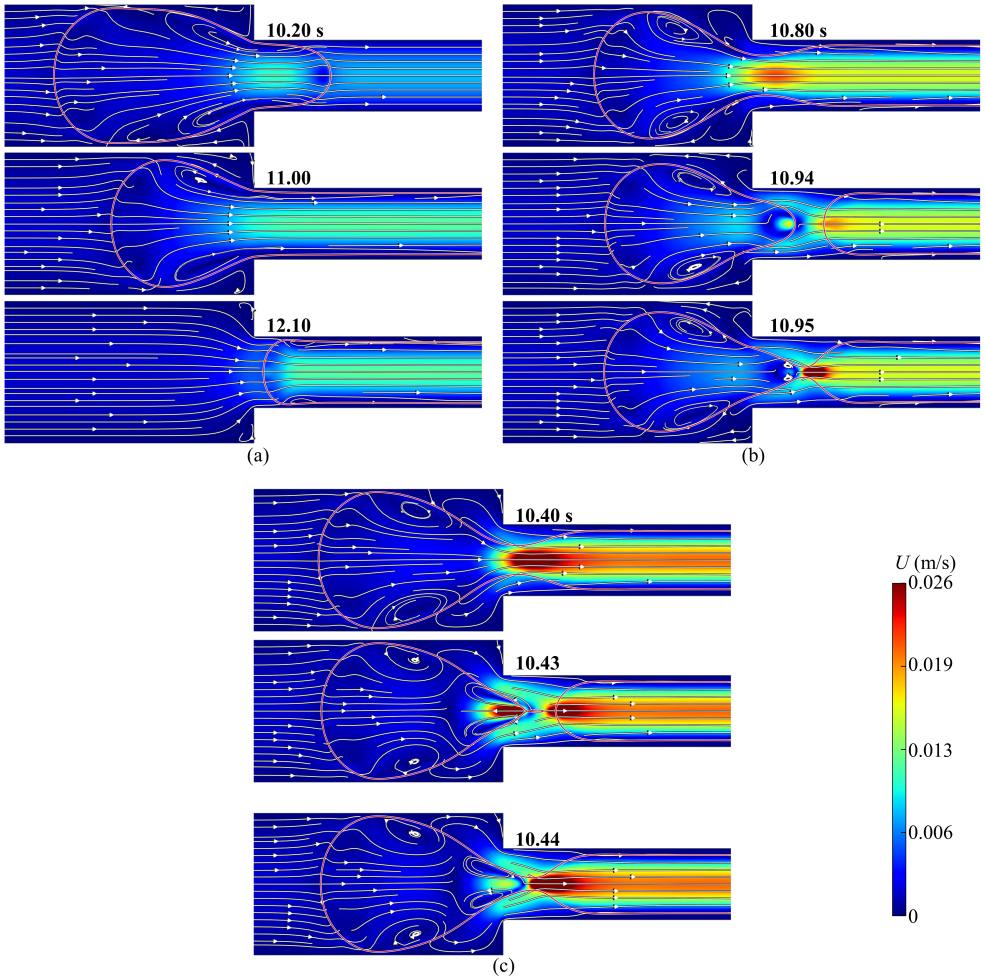



**Figure 11.** Center plane velocity magnitude and streamlines at selected stages for the conditions in Figure 10: (**a**) no breakup at $t = 10.20$, 11.00, and 12.10 s for $Q_3 = 0.78$ mL/h; (**b**) rear-free breakup at $t = 10.80$, 10.94, and 10.95 s for $Q_3 = 3.56$ mL/h; (**c**) rear-confined breakup at $t = 10.40$, 10.43, and 10.44 s for $Q_3 = 6.25$ mL/h. The color contours represent the velocity magnitude, the white lines with arrows represent streamlines, and the red curves indicate the fluid thread interface.

Figure 12 presents the corresponding surface distributions of the normalized mean curvature radius, $\overline{R}_m = R_m/R$, where $R_m$ denotes the mean curvature radius of the fluid thread interface and $R$ is the upstream channel radius. Thus, a smaller $\overline{R}_m$ corresponds to a

larger local mean curvature and a more strongly concentrated capillary response. Before the fluid thread reaches the contraction, relatively large values of $\overline{R}_m$ occupy most of the central interface, whereas smaller values are primarily distributed over the end caps. Passage through the contraction redistributes $\overline{R}_m$ and generates a localized region of low $\overline{R}_m$ at the developing neck. For $Q_3 = 0.78$ mL/h, this region remains bounded and relaxes as the fluid thread recovers without breakup. At $Q_3 = 3.56$ mL/h, it persists after rear detachment and contracts until rear-free pinch off occurs. At $Q_3 = 6.25$ mL/h, the minimum $\overline{R}_m$ remains concentrated adjacent to the contraction, consistent with rear-confined breakup. The distribution of $\overline{R}_m$ therefore connects the center plane flow field to the capillary response in three dimensions; focusing induced by lateral flow determines where the mean curvature is amplified, while rear contact determines whether that amplification remains locked to the contraction.

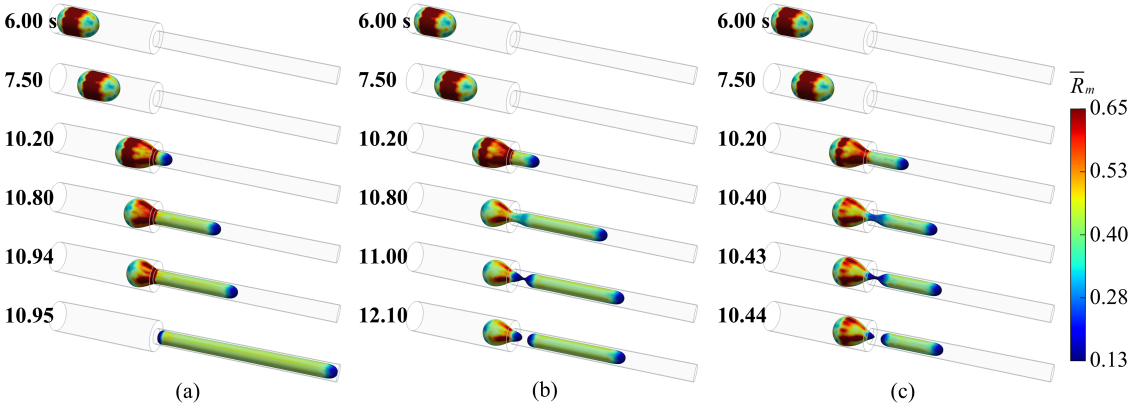



**Figure 12.** Surface distributions of the normalized mean curvature radius $\overline{R}_m = R_m/R$ for the conditions in Figure 10: (**a**) no breakup at $Q_3 = 0.78$ mL/h; (**b**) rear-free breakup at $Q_3 = 3.56$ mL/h; (**c**) rear-confined breakup at $Q_3 = 6.25$ mL/h.

### *3.5. Integrated Breakup Mechanism*

The controlled variation in $Q_3$ links the simulated flow organization to the three-dimensional curvature response. The experimental and numerical results are integrated below to summarize how geometry, external forcing, and rear contact jointly determine the breakup mode.

Taken together, the experiments and simulations identify three coupled elements of the breakup mechanism. First, the sudden contraction creates the capillary disturbance by forcing the fluid thread to redistribute its axial and transverse curvatures. Second, the imposed lateral flow controls whether that disturbance remains reversible or develops into sustained neck collapse. Third, the rear contact state selects the topology of a single breakup event. Detachment before collapse removes direct geometric constraint from the rear and leads to rear-free breakup; persistent contact maintains coupling among the neck, lubrication film, and contraction and leads to rear-confined breakup. At still larger forcing, more than one localized neck can become unstable, giving multiple breakup.

The regime maps, curvature histories, velocity fields, and surface curvature distributions consistently show that no single critical *Ca* is sufficient to characterize the system. The outcome also depends on $\overline{L}$, the contraction ratio, wall wettability, lubrication film thickness, and the order of rear detachment and neck collapse. Within the present geometry, $Q_3$ is an effective control parameter because it reorganizes the local flow and curvature fields and thereby changes the breakup state. These observations provide a mechanistic basis for controlling the breakup of confined fluid threads in sudden contraction microfluidic devices.

## 4. Conclusions

This study combined high-speed imaging with three-dimensional numerical simulations based on the VOF method to examine the interfacial evolution and breakup of confined fluid threads in a circular sudden contraction microchannel. The effects of capillary number, initial fluid thread length, lateral flow rate, and rear wall contact were considered to establish how the contraction geometry and external forcing determine the breakup response. The results identify the coupled geometric and hydrodynamic factors that govern mode selection and provide a basis for controlling fluid thread breakup in confined microfluidic systems.

The experiments identified four responses at low $Ca$, namely no breakup, breakup after rear detachment, breakup under rear confinement, and multiple breakup. Their point distributions depend jointly on $Ca$ and the normalized initial fluid thread length $\overline{L} = L/(2R)$, with the plotted range extending from approximately $\overline{L} = 1.73$–$2.17$ and $Ca = 0.8 \times 10^{-5}$–$8.4 \times 10^{-5}$. Under the representative condition with fixed flow rates, increasing $Q_3$ from 0.30 to 1.00 mL/h by a factor of 3.33 changed the observed response from no breakup to multiple breakup through rear-free and rear-confined breakup. At higher $Ca$, lateral transport and shear broadened the breakup domain and accelerated neck contraction, while the rear contact state continued to distinguish rear-free breakup from rear-confined breakup. The measured curvature dynamics exhibited mode dependent late-stage power laws, with effective exponents of 0.257 and 0.182 for $\overline{R}_1$ and $\overline{R}_m$ after rear detachment, and 0.350 and 0.307 under rear confinement.

The simulations reproduced the principal interfacial topology and the sequence of rear detachment and neck collapse observed in the experimental sequence used for validation. At fixed $\overline{L} = 1.3$ and mean fluid thread velocity $9.23 \times 10^{-4}$ m/s, increasing $Q_3$ from 0.78 to 3.56 and 6.25 mL/h, corresponding to increases by factors of 4.56 and 8.01 relative to the lowest value, drove the progression from no breakup to rear-free breakup and then to rear-confined breakup. The three-dimensional curvature fields showed that the normalized mean curvature radius $\overline{R}_m$ remained finite and relaxed in the no breakup case, migrated downstream after rear detachment during rear-free breakup, and stayed localized near the contraction during rear-confined breakup. These results demonstrate how the numerical flow and curvature fields complement the experiments by resolving the three-dimensional mechanisms that control the breakup location and mode.

**Author Contributions:** Conceptualization, W.W., L.H., S.L. and X.C.; methodology, W.W. and X.C.; software, W.W. and X.C.; validation, W.W. and X.C.; formal analysis, W.W., L.H., S.L. and X.C.; investigation, W.W., L.H., S.L. and X.C.; resources, S.L. and X.C.; data curation, W.W. and X.C.; writing—original draft preparation, W.W.; writing—review and editing, W.W. and X.C.; visualization, W.W., L.H., S.L. and X.C.; supervision, W.W., L.H., S.L. and X.C.; project administration, X.C.; funding acquisition, W.W., L.H. and X.C. All authors have read and agreed to the published version of the manuscript.

**Funding:** This work was partly supported by the National Natural Science Foundation of China (grant nos. 12272050 and U23B6009) and the Fundamental Research Funds for the Central Universities (grant no. 2025CX01001).

**Institutional Review Board Statement:** Not applicable.

**Informed Consent Statement:** Not applicable.

**Data Availability Statement:** The data that support the findings of this study are available from the corresponding author upon reasonable request.

**Conflicts of Interest:** The authors declare no conflicts of interest.

## References

1. Plateau, J. *Experimental and Theoretical Statics of Liquids Subject to Molecular Forces Only*; Gauthier-Villars: Paris, France, 1873.
2. Rayleigh, L. On the Instability of Jets. *Proc. Lond. Math. Soc.* **1878**, *10*, 4–13. [CrossRef]

3. Eggers, J. Nonlinear Dynamics and Breakup of Free-Surface Flows. *Rev. Mod. Phys.* **1997**, *69*, 865–929. [CrossRef]
4. Papageorgiou, D.T. On the Breakup of Viscous Liquid Threads. *Phys. Fluids* **1995**, *7*, 1529–1544. [CrossRef]
5. Lister, J.R.; Stone, H.A. Capillary Breakup of a Viscous Thread Surrounded by Another Viscous Fluid. *Phys. Fluids* **1998**, *10*, 2758–2764. [CrossRef]
6. Driessen, T.; Jeurissen, R.; Wijshoff, H.; Toschi, F.; Lohse, D. Stability of Viscous Long Liquid Filaments. *Phys. Fluids* **2013**, *25*, 062109. [CrossRef]
7. Garstecki, P.; Fuerstman, M.J.; Stone, H.A.; Whitesides, G.M. Formation of Droplets and Bubbles in a Microfluidic T-Junction: Scaling and Mechanism of Breakup. *Lab A Chip* **2006**, *6*, 437–446. [CrossRef]
8. van Steijn, V.; Kleijn, C.R.; Kreutzer, M.T. Predictive Model for the Size of Bubbles and Droplets Created in Microfluidic T-Junctions. *Lab A Chip* **2010**, *10*, 2513–2518. [CrossRef]
9. Anna, S.L.; Bontoux, N.; Stone, H.A. Formation of Dispersions Using Flow Focusing in Microchannels. *Appl. Phys. Lett.* **2003**, *82*, 364–366. [CrossRef]
10. Guillot, P.; Colin, A.; Utada, A.S.; Ajdari, A. Stability of a Jet in Confined Pressure-Driven Biphasic Flows at Low Reynolds Numbers. *Phys. Rev. Lett.* **2007**, *99*, 104502. [CrossRef]
11. Glawdel, T.; Elbuken, C.; Ren, C.L. Droplet Formation in Microfluidic T-Junction Generators Operating in the Transitional Regime. I. Experimental Observations. *Phys. Rev. E* **2012**, *85*, 016322. [CrossRef]
12. Bedram, A.; Moosavi, A.; Kazemzadeh Hannaani, S. Analytical Relations for Long-Droplet Breakup in Asymmetric T Junctions. *Phys. Rev. E* **2015**, *91*, 053012. [CrossRef]
13. Link, D.R.; Anna, S.L.; Weitz, D.A.; Stone, H.A. Geometrically Mediated Breakup of Drops in Microfluidic Devices. *Phys. Rev. Lett.* **2004**, *92*, 054503. [CrossRef]
14. Menetrier-Deremble, L.; Tabeling, P. Droplet Breakup in Microfluidic Junctions of Arbitrary Angles. *Phys. Rev. E* **2006**, *74*, 035303. [CrossRef]
15. Che, Z.; Nguyen, N.T.; Wong, T.N. Hydrodynamically Mediated Breakup of Droplets in Microchannels. *Appl. Phys. Lett.* **2011**, *98*, 054102. [CrossRef]
16. Cubaud, T. Deformation and Breakup of High-Viscosity Droplets with Symmetric Microfluidic Cross Flows. *Phys. Rev. E* **2009**, *80*, 026307. [CrossRef]
17. Huerre, A.; Theodoly, O.; Leshansky, A.M.; Valignat, M.P.; Cantat, I.; Jullien, M.C. Droplets in Microchannels: Dynamical Properties of the Lubrication Film. *Phys. Rev. Lett.* **2015**, *115*, 064501. [CrossRef]
18. Roof, J.G. Snap-Off of Oil Droplets in Water-Wet Pores. *Soc. Pet. Eng. J.* **1970**, *10*, 85–90. [CrossRef]
19. Tsai, T.M.; Miksis, M.J. Dynamics of a Drop in a Constricted Capillary Tube. *J. Fluid Mech.* **1994**, *274*, 197–217. [CrossRef]
20. Datta, S.S.; Dupin, J.B.; Weitz, D.A. Fluid Breakup during Simultaneous Two-Phase Flow through a Three-Dimensional Porous Medium. *Phys. Fluids* **2014**, *26*, 062004. [CrossRef]
21. Beresnev, I.A.; Li, W.; Vigil, R.D. Condition for Break-Up of Non-Wetting Fluids in Sinusoidally Constricted Capillary Channels. *Transp. Porous Media* **2009**, *80*, 581–604. [CrossRef]
22. Wang, X.; Wang, K.; Riaud, A.; Wang, X.; Luo, G. Experimental Study of Liquid/Liquid Second-Dispersion Process in Constrictive Microchannels. *Chem. Eng. J.* **2014**, *254*, 443–451. [CrossRef]
23. Chen, X.; Xue, C.; Hu, G. Confinements Regulate Capillary Instabilities of Fluid Threads. *J. Fluid Mech.* **2019**, *873*, 816–834. . Corrigendum in *J. Fluid Mech.* **2019**, *873*, 1207. [CrossRef]
24. Wang, B.; Zhang, S.; Chen, X. Deformation Dynamics and Breakup Criteria of Confined Fluid Threads in Motion. *Phys. Fluids* **2019**, *31*, 121702. [CrossRef]
25. Wang, B.; Zhang, S.; Chen, X. Shape Evolutions of Moving Fluid Threads under Asymmetrical Confinements. *Phys. Fluids* **2020**, *32*, 042004. [CrossRef]
26. Hirt, C.W.; Nichols, B.D. Volume of Fluid (VOF) Method for the Dynamics of Free Boundaries. *J. Comput. Phys.* **1981**, *39*, 201–225. [CrossRef]
27. Rider, W.J.; Kothe, D.B. Reconstructing Volume Tracking. *J. Comput. Phys.* **1998**, *141*, 112–152. [CrossRef]
28. Harvard Apparatus. *Pump 11 Elite and Pump 11 Pico Plus Elite Series Syringe Pump User's Manual*; Publication 5420-002, Revision A; Harvard Apparatus: Holliston, MA, USA, 2010.
29. Deshpande, S.S.; Anumolu, L.; Trujillo, M.F. Evaluating the Performance of the Two-Phase Flow Solver interFoam. *Comput. Sci. Discov.* **2012**, *5*, 014016. [CrossRef]
30. Brackbill, J.U.; Kothe, D.B.; Zemach, C. A Continuum Method for Modeling Surface Tension. *J. Comput. Phys.* **1992**, *100*, 335–354. [CrossRef]


**Disclaimer/Publisher's Note:** The statements, opinions and data contained in all publications are solely those of the individual author(s) and contributor(s) and not of MDPI and/or the editor(s). MDPI and/or the editor(s) disclaim responsibility for any injury to people or property resulting from any ideas, methods, instructions or products referred to in the content.